Journal of Computational Physics 397 (2019) 108790

Contents lists available at ScienceDirect

Journal of Computational Physics

www.elsevier.com/locate/jcp

A massively-parallel, unstructured overset method to simulate moving bodies in turbulent flows

Wyatt James Horne, Krishnan Mahesh *

University of Minnesota, Department of Aerospace Engineering and Mechanics, Minneapolis 55414, USA

ARTICLE INFO

Article history:
Received 29 January 2019
Received in revised form 25 June 2019
Accepted 26 June 2019
Available online 12 July 2019

Keywords:
Unstructured
Overset
DNS
LES
Conservative
Parallel

ABSTRACT

An unstructured overset method capable of performing direct numerical simulation (DNS) and large eddy simulation (LES) of many ($O(10^5)$) moving bodies, utilizing many computational cores ($O(10^5)$), in turbulent, incompressible fluid flow is presented. Unstructured meshes are attached to bodies and placed within a fixed background domain. Body meshes are allowed to arbitrarily overlap and move throughout the domain. Within each mesh a high resolution, unstructured, non-dissipative finite volume method is used to solve for the flow field. Boundary conditions for each mesh are provided by interpolation from flow solutions on overlapping meshes. When many unstructured meshes of different resolution overlap, care is required in the connection between the different flow solutions. An interpolant is created which seeks to preserve volume conservation of flow quantities between meshes regardless of overlapping mesh differences. An implicit fractional step method is used for time advancement, requiring the calculation of a predicted fluid velocity and corrector pressure field. For the predictor step, the resulting interpolation is directly introduced into the implicit equations for the predicted flow field. For the corrected pressure field, the continuity between meshes is weakly enforced using a penalty formulation. The pressure formulation is symmetric, positive-definite and non-singular resulting in a formulation which is readily solvable using traditional iterative matrix inversion techniques. An Arbitrary Euler-Lagrangian (ALE) method coupled to a 6 degrees of freedom rigid body equation system (6-DOF) is used for body motion. For rotation, a quaternion representation is used to solve Euler's equations of rigid body motion. A linear spring damper model, which uses geometry information readily available from the overset assembly process, is used for collisions. Validation of the method for canonical flow fields is presented including assessment of order of accuracy and kinetic energy conservation properties. Particle-resolved direct numerical simulation (PR-DNS) of single particles in various flow fields are presented for validation. PR-DNS results of 50,000 spherical particles freely moving within turbulent channel flow are shown as a demonstration of the method at full scale. LES results of a marine propeller under crashback conditions are shown to demonstrate the ability to simulate highly unsteady turbulent flows over complex, moving geometries.

* Corresponding author.
E-mail address: kmahesh@umn.edu (K. Mahesh).

https://doi.org/10.1016/j.jcp.2019.06.066
0021-9991/

1. Introduction

Many engineering devices and natural fluid flows feature multiple moving bodies within turbulent fluid. Turbulent particle-laden flow is commonly found in gas-turbine aircraft engines, solid-particle solar receivers, ocean sediment transport and dust or sand transport in the atmosphere [1–3]. Such flows display a large range of scales ranging from large convective scales down to flow scales smaller than individual particles. For example, in sand or dust transport in the atmosphere, particulates are $O(1-100)$ microns in size and the large convective scales are of the scale of the atmospheric turbulent boundary layer ($O(100-1000)$ meters) [4]. Understanding the dynamics of fluid flow with length scales smaller than individual particles, and their interaction with larger scales, is necessary to understand the dynamics of the full fluid-solid system. Interface-resolved or particle-resolved direct-numerical-simulations (PR-DNS) [5], seek to directly resolve both, convective scales and scales much smaller than particles [6–8].

Numerical methods which can perform PR-DNS of moving particles in turbulent flows must be capable of accurately resolving many moving body surfaces in a turbulent fluid flow. The motion of these boundaries is generally not known *a priori*, and hence the methods must be dynamic in time for general motion. To dynamically represent the surfaces of the particles two strategies are commonly used: methods which use body-fitted meshes attached to particles [9–14] and non-conforming methods which impose the moving particle boundary conditions on a fixed, typically Cartesian mesh [15,8,16–18]. In a body-fitted method, either the entire solution domain must be re-meshed dynamically as particles move through the domain or the mesh solutions must be connected via a procedure akin to overset methods [19]. Non-conforming methods, such as Immersed Boundary Methods (IBM) or Fictitious domain methods [20,15,21–24], avoid these difficulties by instead adding forces or constraints to the governing equations of motion which yield the desired moving boundary conditions.

IBM is an example of a non-conforming method which has been used to perform PR-DNS of turbulent particle-laden flow [16,7]. In IBM a force is added to the governing equations to impose non-conforming boundary conditions. This type of method is relatively efficient and is generally easier to implement relative to a body-fitted, re-meshing method, e.g. Patankar et al. [13], Choi and Joseph [14]. Using IBM, challenging PR-DNS problems such as surface-resolved sediment bed erosion have been investigated [7]. One disadvantage of IBM is the necessity of high resolution in the vicinity of moving boundaries, especially for high Reynolds numbers (Re) [24,22]. High resolution must be placed in locations near moving boundaries, which are often unknown, or the mesh must be adaptively refined near the boundaries of particles, which has similar disadvantages to re-meshing methods. Often in place of adaptive refinement, the entire mesh is set to an adequate resolution to resolve the particles. This can result in large, non-optimal meshes with unnecessarily high resolution over much of the domain.

In addition, the calculation of forces and other quantities on the moving bodies requires a reconstruction operation where flow field quantities must be accurately recreated along the surfaces of bodies. This reconstruction is often conducted at Lagrangian points along body surfaces. The placement of these points along the surface is non-trivial in that the nearby, possibly non-uniform, mesh resolution must be reflected in the placement of the points. In simulations of PR-DNS several moving surfaces can be present within a single volume depending on the resolution of the fixed mesh. This can create a non-trivial constraint on the fluid flow such that none of the moving boundary conditions can be imposed accurately.

In body-fitted methods it is possible to ensure adequate resolution at the surfaces of particles with conforming meshes that do not require reconstruction or Lagrangian point placement for force calculations. If an overset methodology is used, it is also possible to avoid the necessity of adaptive mesh refinement or large, non-optimal meshes. It also avoids much of the cost found in a full re-meshing method since only the connectivity between meshes is dynamic. In an overset method meshes are directly attached to surfaces and allowed to arbitrarily overlap and move throughout the solution domain [25,19]. A key challenge of an overset method is connecting the solutions between meshes robustly, efficiently and accurately throughout the domain. Mesh cells can be located exterior to the solution domain and must be removed from the simulation. Additionally, there may be regions in the domain where many meshes overlap and redundant solutions exist. For best efficiency, cells within these regions must be selectively removed to reduce the redundancy while covering the entire domain. Boundaries remain at the edges of overset meshes and regions of removed cells, which must be supplied boundary conditions reconstructed from other meshes.

Overset and body-fitted methods in general have seen limited application to PR-DNS. The number of particles is generally low and the cases studied are relatively simple compared to what has been achieved by non-conforming methods. One reason for this is the inherent difficulty in scaling up the necessary connectivity calculations for overset to large numbers of meshes and computational cores. In our recent work, an overset method was developed to address this issue [26]. The method was shown to be capable of performing connectivity calculations for large numbers of meshes on large numbers of cores. In particular, strong-scaling was demonstrated for 100,000 spherical particles moving within a turbulent channel flow [26].

Another difficulty when using an overset method is conservation and interpolation error, especially when many overlapping meshes are present with potentially differing resolutions. In particular, mass conservation has been a long standing issue in overset methods when solving for incompressible fluid flow [27]. While some approaches have been presented for the conservation issues of overset, e.g. Wang [28], they are generally ad-hoc (e.g. arbitrarily adding mass over an entire mesh), numerically intractable for large numbers of meshes, or untenable for an accurate calculation when many, varied meshes overlap. To address interpolation error, a common strategy is to employ an interpolation which is of higher order

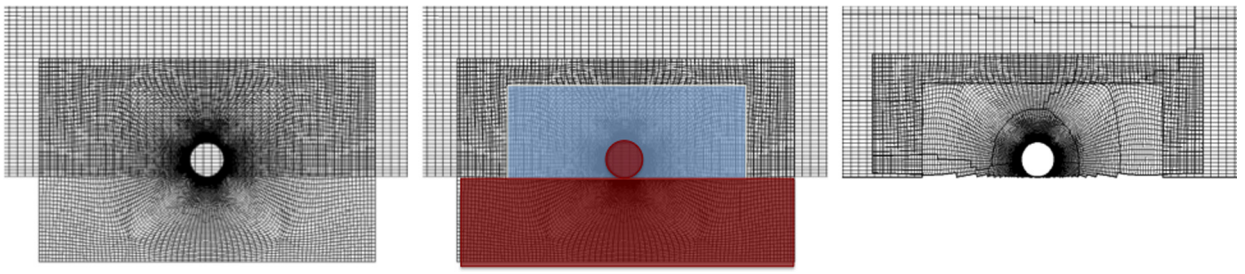

Fig. 1. Spherical particle near wall overset example before and after cutting using an angled rectangular box primitive shape from Horne and Mahesh [26]. Blue (■) regions indicate a region where overlap must be reduced. Red (■) regions indicate elements that lie within solid boundaries. Note that elements on the background channel mesh within the particle and (■) are removed and elements on the particle mesh below the channel wall are removed. (For interpretation of the colors in the figure(s), the reader is referred to the web version of this article.)

than the base method. This is non-optimal since it requires the creation of much larger numerical stencils than is required for the overall order of accuracy of the base method. It also does not address differences in mesh resolution along overset interpolation boundaries which could potentially produce error.

In this work, we present an overset method which seeks to improve conservation errors when many meshes are present while also producing a result which maintains the accuracy of the base fluid method for incompressible flow. The goal for the method is to successfully perform DNS and large eddy simulation, LES, of many moving bodies in turbulent fluid flow, with PR-DNS being the primary example explored here. In Sec. 2 the method for solving fluid motion is presented including details of the necessary interpolation. Sec. 3 shows details of the solid body motion including the collision strategy. Validation results for the method are shown as appropriate in each section. Sec. 4 shows validation for single particles in a variety of flow fields and an example of a large-scale calculation using the method. The example chosen for this work is 50,000 particles in a turbulent channel flow. LES of a marine propeller under crashback conditions is then presented to illustrate the method's ability to simulate highly unsteady turbulent flows over complex geometries.

2. Fluid phase

To perform an overset simulation, multiple meshes are placed within a domain and allowed to arbitrarily overlap. The solutions between the different meshes are connected through an overset assembly process. The present method uses the assembly process described in Horne and Mahesh [26]. Fig. 1 depicts the assembly process for a spherical particle at a wall. When meshes overlap control volumes are dynamically found outside the solution domain, shown in the red region in the figure, and must be removed from the simulation dynamically as particles move. In regions where meshes overlap, redundant solutions are present. Control volumes within these regions are removed as possible for improved efficiency. After control volumes have been removed, exposed surfaces remain which must be provided boundary conditions. The solution from overlapping meshes that overlap these surfaces provide boundary conditions through interpolation. To apply the boundary conditions control volumes next to interpolation boundaries are treated as ghost cells which are provided values through interpolation.

The motion of the fluid phase is modeled using the incompressible Navier-Stokes equations. For movement, an arbitrary Lagrangian-Eulerian (ALE) formulation of the equations is used. The ALE formulation avoids tracking multiple reference frames for arbitrary motion of meshes through the inclusion of the mesh velocity in the convection term.

$$\int_{\Omega} \frac{\partial u_i}{\partial t} dV + \int_{\partial\Omega} (u_i (u^n - u^n_{mesh}) dA) = -\int_{\Omega} \frac{1}{\rho} \frac{\partial p}{\partial x_i} dV + \int_{\partial\Omega} \nu \frac{\partial u_i}{\partial n} dA \tag{1}$$

$$\int_{\partial\Omega} u^n dA = 0 \tag{2}$$

The equations are integrated over an arbitrary control volume Ω, with faces $\partial\Omega$ which have normals n. Here, u_i is the inertial fluid velocity in the ith Cartesian direction, u^n is the inertial velocity normal to the faces of the control volume, u^n_{mesh} is the velocity of the mesh normal to the faces of the control volume, p is the pressure, and ρ is the fluid density. To discretize these equations a non-dissipative, high resolution, unstructured finite volume scheme which focuses on kinetic energy conservation based on Mahesh et al. [29] is used.

The use of unstructured meshes allows for flexibility in the placement of high resolution where desired in a simulation. Non-dissipative finite volume schemes which conserve discrete kinetic energy have been found to be effective at performing LES of high Re fluid flows [30,29]. In particular, the energy cascade, which is an essential physical process in turbulent fluid flow, has been found to have improved accuracy when a kinetic energy conserving scheme is utilized [31,30]. In addition to accuracy, for a method to be robust it is necessary that the total kinetic energy within a simulation domain be bounded in

the inviscid limit for all time. When discrete kinetic energy is conserved this property is obtained so long as the boundary conditions for the fluid flow are bounded.

Within each mesh, Eq. (2) is spatially discretized as

$$\frac{\partial u_{i,cv}}{\partial t}dV_{cv} + \sum_{faces}\frac{(u_{i,cv}+u_{i,nbr})}{2}(u^n - u^n_{mesh})dA_f - \sum_{faces}\nu\frac{(u_{i,nbr}-u_{i,cv})}{d_f}dA_f = -\frac{1}{\rho}\frac{\partial p_{cv}}{\partial x_i}dV_{cv} \tag{3}$$

$$\sum_{faces} u^n dA_f = 0 \tag{4}$$

where $u_{i,cv}$ is the piecewise constant flow velocity using Cartesian index i, dV_{cv} is the volume of the control volume, $u_{i,nbr}$ is a neighboring control volume's velocity, dA_f is the area of the face between control volumes, d_f is the distance between centroids of neighboring control volumes, p_{cv} is the piecewise constant pressure.

To assess the kinetic energy properties of the formulation we begin with the case where $\nu = 0$ and $\frac{\partial p_{cv}}{\partial x_i} = 0$. Multiplying Eq. (4) by $u_{i,cv}$ and integrating over a mesh yields

$$\sum_{cvs}\frac{\partial \frac{u_{i,cv}u_{i,cv}}{2}}{\partial t}dV_{cv} + \sum_{i.+b.faces}\frac{u_{i,cv}u_{i,nbr}}{2}(u^n - u^n_{mesh})dA_f = 0 \tag{5}$$

Where $i.+b.\ faces$ refers to faces around interpolation boundaries and solid boundaries, and $\sum_{faces}(u^n - u^n_{mesh})dA_f = 0$ was used, assuming incompressible flow and rigid body motion. As can be seen in the expression, only boundaries contribute to the change in total kinetic energy within a mesh for this case. If the kinetic energy provided by interpolation and solid boundaries is bounded the method will be robust without any necessary added dissipation. Using a non-zero, positive value of ν will not negatively impact this robustness. A non-zero $\frac{\partial p_{cv}}{\partial x_i}$ can negatively influence the result unless care is taken in its construction. To further analyze the energy behavior when $\frac{\partial p_{cv}}{\partial x_i}$ is non-zero, the full equation system must be assessed.

The rotational correction incremental scheme first presented by Timmermans et al. [32] and later analyzed by Guermond and Shen [33] is used for time advancement due to its improved numerical accuracy relative to other incremental pressure schemes. Using a trapezoidal time integration the method can be written as

$$\begin{aligned}
&\frac{u^*_{i,cv} - u^{k-1}_{i,cv}}{dt} + \frac{1}{2}(CONV^* + CONV^{k-1}) + \frac{1}{2}(VISC^* + VISC^{k-1}) = -\frac{\partial p^{k-1}_{cv}}{\partial x_i} + F_{b,i},\\
&u^{*,n} = \frac{u^*_{i,cv} + u^*_{i,nbr}}{2}n_i,\\
&u^{*,n,int} = (u^*_{i,cv} + \frac{\partial u^*_{i,cv}}{\partial x_j}\Delta x_{j,face})n_i
\end{aligned} \tag{6}$$

$$\begin{aligned}
&\sum_{faces} u^{*,n}dA_f = dt\sum_{faces}\frac{\partial \phi^k_{cv}}{\partial n}dA_f,\\
&\frac{u^{k,n} - u^{*,n}}{dt} = -\frac{\partial \phi^k_{cv}}{\partial n},\\
&\frac{u^k_{i,cv} - u^*_{i,cv}}{dt} = -\frac{\partial \phi^k_{cv}}{\partial x_i},\\
&p^k_{cv} = \phi^k_{cv} + p^{k-1}_{cv} - \nu\nabla\cdot u^*_{cv}
\end{aligned} \tag{7}$$

where Eq. (6) is the predictor step and Eq. (7) is the corrector step. In the equations, u^{k-1}, p^{k-1} indicate the flow field from the previous time step, dt indicates the discrete time step, $CONV$ and $VISC$ correspond to the discretized convection and viscous terms in the equation, and $F_{b,i}$ is a general conservative body force. The fluid density has been included in p_{cv} for simplicity. The predicted convection face velocity, indicated as $u^{*,n}$, is calculated using an arithmetic mean of the predicted velocity field dotted with the face normal n_i. A one-sided least squares reconstruction is instead used to calculate the predicted convection face velocity, $u^{*,n,int}$, using the vector from the CV centroid to the face centroid, $\Delta x_{j,face}$. The pressure equation uses gauge variable ϕ^k_{cv}, defined according to the difference in pressure between time steps and the divergence in the predicted velocity field. The corrected convection face velocity, $u^{k,n}$ is obtained from the normal gradient of ϕ at each face and $u^{*,n}$. The resulting fluid velocity, $u^k_{i,cv}$, is obtained by correcting the predicted velocity using a reconstructed gradient of the gauge variable.

The mesh velocity is assumed to be linear between time steps and defined as $u^n_{i,mesh} = (x^k_{i,cv} - x^{k-1}_{i,cv})n_i/dt$ where $x^k_{i,cv}$ is a control volume centroid at different time levels as found by solid body motion. This selection exactly reconstructs a linear

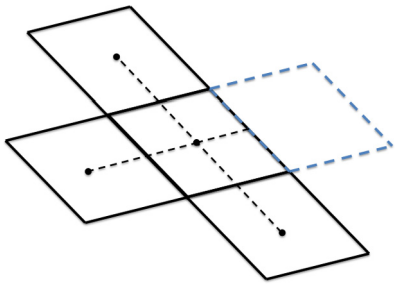

Fig. 2. Example $\overline{u}^{*,n,int}$ reconstruction stencil near interpolation boundary. Control volumes (–) are used to construct a LSQ stencil (- -) to provide a value for $\overline{u}^{*,n}$ for the face connected to the interpolation control volume (- -). Note that the interpolated control volume value is not part of the stencil and does not contribute directly to the face value.

flow solution over the mesh motion regardless of displacement so long as the mesh is of reasonable quality. To illustrate, consider a mesh moving arbitrarily in a flow with one non-zero velocity component defined as $u_1 = ax_2 + b$, $u_2 = u_3 = 0$, where only convection is considered. The discretized equations can be written as:

$$\frac{\partial u_{i,cv}}{\partial t} dV_{cv} + \sum_{faces} \frac{(u_{i,cv} + u_{i,nbr})}{2} (u^n_{mesh}) dA_f = \frac{\partial u_{i,cv}}{\partial t} dV_{cv} + \frac{\delta u_{i,cv}}{\delta x_{j,cv}} u_{j,mesh} dV_{cv} \tag{8}$$

where $\frac{\delta u_i}{\delta x_j}$ is a gradient reconstruction using the Green-Gauss theorem. For a high quality mesh, this reconstruction will be $O(\Delta x^2)$ and thus capable of reconstructing a straight line solution exactly such that $\frac{\delta u_1}{\delta x_2} = a$. If $u_{i,mesh} = (x^k_{i,cv} - x^{k-1}_{i,cv})/dt$ is used then

$$\begin{aligned} &\frac{u^k_{1,cv} - u^{k-1}_{1,cv}}{dt} dV_{cv} + a \frac{x^k_{2,cv} - x^{k-1}_{2,cv}}{dt} dV_{cv} = 0, \\ &u^k_{1,cv} = u^{k-1}_{1,cv} + a(x^k_{2,cv} - x^{k-1}_{2,cv}) = a x^k_{2,cv} + b \end{aligned} \tag{9}$$

which is an exact result. This is an important result that shows the discretized ALE will be accurate so long as the flow solution is approximately linear over the motion of the mesh between time steps. In numerical tests using the cases presented later in this work it is found that this is not a hard limit on the time advancement of the method, but can serve as a guideline for selecting time step size.

The reconstruction of the convective face velocity at interpolation boundaries plays an important role in the accuracy of pressure. When under-resolved, $\overline{u}^{*,n,int}$ can have non-trivial error which produces poor pressure behavior if a centrally averaged value is used. Spurious pressure values can be introduced which can produce unrealistic pressure forcing on bodies moving in turbulence. A least squares, LSQ, reconstruction is used for $\overline{u}^{*,n,int}$ instead of a central average at interpolation boundaries when conducting LES. The LSQ reconstruction is performed using control volumes which do not receive an interpolated value near interpolation boundaries as depicted in Fig. 2. This effectively lessens the influence interpolated fluid velocity values have on the resulting pressure solution which can provide substantial improvements to pressure solutions within an overset mesh. Note that the LSQ reconstruction is only performed at interpolation boundaries and a central average is still used throughout the interior of all meshes. Further note that when the flow solution on all meshes is fully resolved, or sufficiently smooth, the use of the LSQ reconstruction at interpolation boundaries is unnecessary and a simple central average can be used instead. This was found to be the case in numerical experiments of DNS/LES.

To illustrate the improvement in pressure using the proposed $\overline{u}^{*,n,int}$ construction, simulations are performed of a marine propeller as described in Sec. 4.5. Fig. 3 shows 100 time steps of side forcing information on the shaft and propeller using a centrally averaged and LSQ reconstructed values of $\overline{u}^{*,n,int}$ at interpolation boundaries. As can be seen in the non-dimensional RMS of side forces, K_s, significant spurious, point-to-point, pressure forcing is found in the centrally averaged result whereas the resulting side forces are smooth and well-behaved with LSQ reconstruction. Over time the introduced spurious values of K_s, using central averaged values, generate high frequency modes in the side force spectra which are not found in experimental data. The relatively smooth solution found using the LSQ reconstruction matches the behavior found in previous simulations of the case and does not exhibit these spurious high frequency modes [34,35].

Multiplying the equation for the corrected convection face velocity by $u^{k,n}$ and integrating over an entire mesh results in

$$\sum_{dom.faces} \frac{\partial}{\partial t} \left(\frac{u^{k,n} u^{k,n}}{2} dA_f d_f \right) = - \sum_{i.+b.} u^n \phi_f dA_f \tag{10}$$

where the expression includes all faces within a mesh, ϕ_f is the value of the gauge variable at the boundary faces and $\sum_{faces} u^{k,n} dA_f = 0$. This indicates that the total discrete kinetic energy of the convective face velocities is conservative

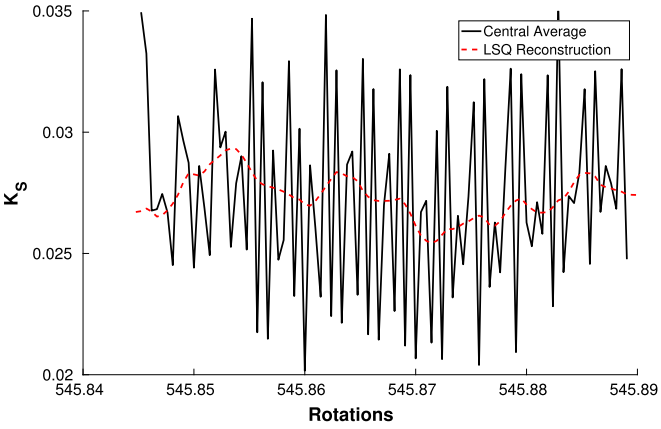

Fig. 3. Comparison of non-dimensional side force RMS with centrally averaged $\overline{u}^{*,n}$ and LSQ reconstructed $\overline{u}^{*,n}$ at overset interpolation boundaries.

within a mesh and bounded if the boundary contribution is bounded. To obtain the same property for the cell-center velocity, $u^k_{i,cv}$, after applying the pressure correction, a least-squares minimization is performed following Mahesh et al. [29] to ensure that for each control volume

$$\sum_{faces}(\frac{\partial\phi}{\partial x_i}n_i - \frac{\partial\phi}{\partial n})dA_f = 0. \tag{11}$$

As shown in their work, this reconstruction ensures that the discrete energy properties found for the convection face velocities are found in a least-squares sense for the corrected control volume fluid velocity.

From the kinetic energy it is clear that the selection of boundary conditions, including interpolation boundaries, for the equations is critical for the overall robustness of the method. It is desirable that flow values at interpolation boundaries be bounded such that kinetic energy is not erroneously introduced between meshes. When a direct interpolation is used, particularly when meshes are of significantly different resolution, this can be non-trivial to achieve. As one example, interpolating a discrete, test sinusoid function between meshes can result in an increase of discrete kinetic energy if a linear least-squares reconstruction is performed using only one computational stencil, termed local LSQ here, as shown in Fig. 4. In this case kinetic energy will be generated between meshes. In addition to being inaccurate this could be unstable for high Reynolds numbers since the dissipation of kinetic energy due to viscous diffusion is possibly smaller than the generation due to interpolation.

In order to address this potential source of instability a supercell reconstruction is used for all interpolation. The reconstruction is shown in Fig. 5 for a 2D case where the black (■) control volumes are providing an interpolation to the blue (■) ghost cell. The supercell is constructed from all control volumes which intersect a ghost cell. To perform the construction for a general flow variable, ξ, we require that

$$\int_{\Omega,sc}\xi dV = \sum_{o.cv}\int_{\Omega,o.cv}\xi dV \tag{12}$$

where the volume integral of the variable over the supercell, labelled as sc, is equal to the integral over all control volumes which overlap the ghost cell, each denoted $o.cv$. Assuming that ξ is a linear function between a control volume and its neighbors, found using linear least squares, the relation can be discretely satisfied using

$$\begin{aligned}\xi_{cc,sc} &= \frac{\sum_{o.cv}\xi_{cc}dV_{cv}}{\sum_{o.cv}dV_{cv}}\\ \frac{\partial\xi_{cc,sc}}{\partial x_i} &= \frac{\sum_{o.cv}\frac{\partial\xi_{cc}}{\partial x_i}dV_{cv}}{\sum_{o.cv}dV_{cv}}\end{aligned} \tag{13}$$

where ξ_{cc} is the centroid value of the variable and $\frac{\partial\xi_{cc}}{\partial x_i}$ is gradient, both found using a linear LSQ reconstruction, and $\xi_{cc,sc}$ is the corresponding reconstructed values for the supercell.

To perform the interpolation between the supercell and interpolation ghost cell

$$\xi_{cc,gc} = \xi_{cc,sc} + \frac{\partial\xi_{cc,sc}}{\partial x_i}\Delta x_i \tag{14}$$

where $\xi_{cc,gc}$ is the interpolated value and Δx_i is the vector from the centroid of the supercell to the centroid of the ghost cell as shown in the figure. Since the gradient and centroid value of the supercell are volume averages of the contributing

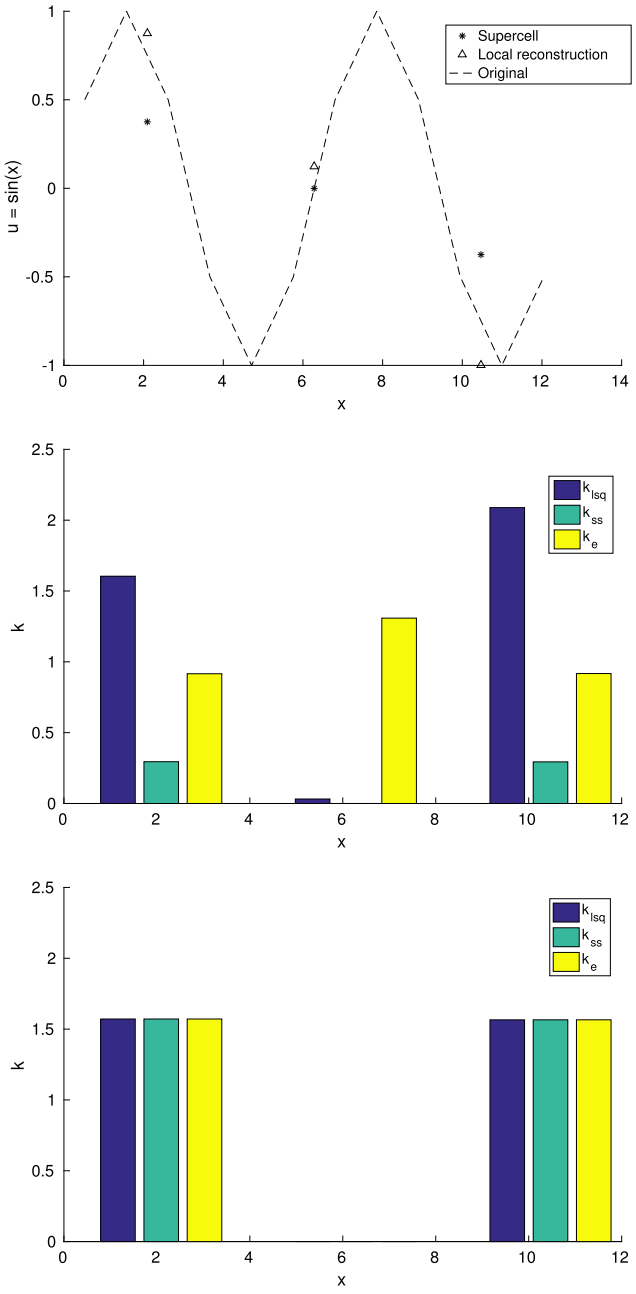

Fig. 4. Interpolation of a discrete sinusoid signal to three control volumes using different reconstructions. In the top figure the original signal and resulting centroid values are shown for different reconstructions. Note that local LSQ has the potential to overshoot the original signal which creates energy while the supercell reconstruction stays bounded. Kinetic energy, $k = \int 1/2 uudV$, is shown for two different sinusoid resolutions in the next two figures. In the middle figure the resolution of the sinusoid is four times as resolved as the three control volumes. As can be seen, kinetic energy is generated in the local LSQ result. Three control volumes are used for the sinusoid in the last result. The kinetic energy is found to be conserved between the original signal and the resulting interpolations when resolution and position are matched.

interpolation control volumes they are both bounded by the interpolation control volume values. Looking at the resulting kinetic energy from this interpolation for the same example test function with increasing resolution of the ghost cells in Fig. 4, it is found that the discrete kinetic energy is bounded. When the meshes are significantly different in resolution the kinetic energy of flow scales smaller than the ghost cell is significantly reduced in the interpolated solution. As the ghost cells approach the same resolution as the overlapping control volumes the resulting discrete kinetic energy approaches equality between the two meshes. In the limits of DNS, where the flow solution is resolved on all meshes present, the discrete kinetic energy is expected to be approximately the same between the meshes along interpolation boundaries. In

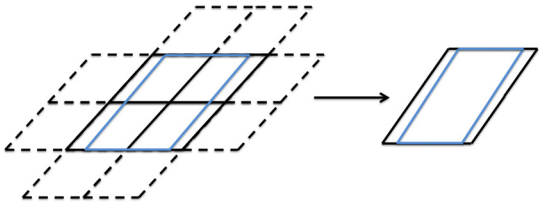

Fig. 5. Example interpolation stencil for a supercell. Overlapping control volumes (–) are used to construct the value and gradient within a combined supercell to interpolate to a ghost cell (–). For the gradient reconstruction, neighbors of the overlapping control volumes are additionally used (- -).

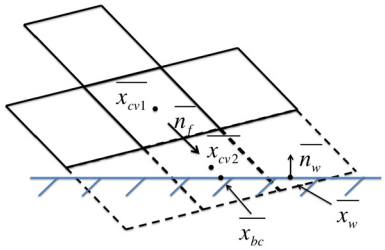

Fig. 6. Example reconstruction for a ghost cell. Non-cut control volumes (–) and the nearby solid boundary (–) are used to reconstruct values in cut control volumes (- -). The face normals along the cut boundary are used to establish points along the solid boundary to enforce the boundary condition. Here, $\overline{n_f}$, $\overline{x_{cv1}}$, $\overline{x_{cv2}}$, $\overline{x_w}$ and $\overline{n_w}$ are used to find $\overline{x_{bc}}$. Once $\overline{x_{bc}}$ is known, linear least squares is conducted using $\overline{x_{cv1}}$, its non-cut neighbors, and $\overline{x_{bc}}$.

addition to this desirable property, the interpolant is spatially 2^{nd} order which matches the overall order of the method for high quality meshes.

There are special cases where it is not possible to construct a supercell as needed for interpolation. For a particle approaching a wall, as shown in Fig. 1, there are exposed interpolation boundaries which have no overlapping meshes present. In such cases there is always a solid boundary present. Geometry information readily available from the overset assembly process is used to reconstruct the nearby boundary condition from the solid boundary on the non-overlapping mesh. To impose the boundary condition a ghost cell method similar to the work of Tseng and Ferziger [20] is used. Fig. 6 shows an example of interpolation ghost cells (–) which require a reconstruction condition from a non-aligning wall (–). To enforce the boundary condition, flow values are set in the cut control volumes (- -) which are then treated as ghost cell boundary conditions. To find the appropriate value, a vector is created between the ghost cell and cut neighboring control volume. Using n-t coordinates along this vector, the t coordinate location on the nearest face of the solid boundary is found using

$$\begin{aligned}
\overline{x} &= (1-t)\overline{x_{cv1}} + t\overline{x_{cv2}}, \\
t_w &= \frac{\overline{x_w}\cdot\overline{n_w} - \overline{x_{cv1}}\cdot\overline{n_w}}{(\overline{x_{cv2}} - \overline{x_{cv1}})\cdot\overline{n_w}}, \\
x_{bc} &= (1-t_w)\overline{x_{cv1}} + t_w\overline{x_{cv2}},
\end{aligned} \tag{15}$$

where $\overline{x_{cv}}$ corresponds to the centroid of a control volume, $\overline{x_w}$ is the solid boundary face centroid, t is the tangential coordinate along a vector from $cv1$ to $cv2$, t_w is the tangential location of the solid boundary, x_{bc} is the location where the solid boundary condition will be enforced, and $\overline{n_w}$ is the normal vector of the solid face as depicted in Fig. 6. A linear LSQ reconstruction is then performed to provide a value for cut control volumes, $cv2$ in the figure, using the flow values and centroids of $cv1$, its neighbors, and the solid boundary at location $\overline{x_{bc}}$ to construct a Vandermode matrix. The Vandermode matrix is inverted to provide weights which can produce the reconstructed values. By using n-t coordinates along $\overline{n_f}$ the least-squares reconstruction is well conditioned, provided that the mesh is of reasonable quality. This has been found to be an important property when using general unstructured meshes which may produce ill-conditioned least-squares reconstructions for arbitrary meshes and overlapping walls.

The resolution of the solid boundary will in general not match the resolution of control volumes which need this reconstruction. In cases where the solid boundary is finer than the nearby control volume resolution, all face centroids, face normals, and boundary conditions which overlap a cut control volume are averaged to give an effective boundary to compute t_w and perform the reconstruction.

The Dirichlet velocity value of the solid boundary is imposed using a linear LSQ reconstruction including the wall to provide a value for the cut control volume. For pressure it is desired to impose $\frac{\partial \phi}{\partial n_w} = 0$. A simplified reconstruction is performed where $\frac{\partial \phi}{\partial n_f} = 0$ is used, with n_f as indicated in the figure. This results in a symmetric, positive-definite matrix for the pressure equation matrix, as will be discussed, with a potential loss in accuracy. The case shown in Fig. 1 is an extreme example selected to show many control volumes which would require the boundary reconstruction. In general

overset meshes are constructed and resolutions for a given case are selected such that only a handful of control volumes will need the reconstruction. Additionally, for PR-DNS and many cases the constraint is only present in near-wall regions which will typically have high resolution such that the error introduced by this selection will be minimal.

When solving for the predicted velocity field in Eq. (6) the interpolation weights and reconstruction weights are directly introduced into the corresponding matrix rows for ghost cells. In numerical tests this has been found to yield a readily solvable system using traditional iterative solution techniques.

The equation for ϕ, as shown in Eq. (7), presents issues when interpolation weights are directly introduced into the matrix. The resulting system is singular, non-symmetric, and possibly non positive definite, noting that $\frac{\partial \phi_{bc}}{\partial n} = 0$. Convergence of this system is difficult and possibly infeasible using traditional iterative methods depending on the case. This can result in $|\sum_{i.+b.} u^{k,n} dA_f| >> 0$ which affects the stability and accuracy of the method.

To address these issues a penalty formulation is used which constrains the pressure solution along interpolation boundaries to match between meshes. Starting from the unconstrained pressure equation

$$\begin{aligned} &\sum_{faces} \frac{\phi_{nbr} - \phi_{cv}}{d_f} dA_f = \sum_{face} u^{*,n} dA_f, \\ &\sum_{i.+b.faces} \frac{\phi_{nbr} - \phi_{cv}}{d_f} dA_f = 0, \end{aligned} \tag{16}$$

where $\frac{\partial \phi}{\partial n} = 0$ at interpolation boundaries and dt has been included in ϕ, a penalty function is introduced at interpolation boundaries and to all control volumes which provide an interpolation value. The Courant quadratic penalty function is used such that when the entire system is solved, the interpolation error between meshes is minimized. Here, the interpolation constraints are taken in matrix-vector form as $\bar{\alpha_p} \cdot \bar{\phi} = 0$, where p is one interpolation equation as found by Eq. (14). Introducing the Courant penalty energy function as

$$\bar{\bar{C}} = \sum_{i.const} \bar{\bar{C_p}}, \bar{\bar{C_p}} = \bar{\phi^t}(1/2\gamma_p \bar{\alpha_p^t} \bar{\alpha_p} \bar{\phi}) \tag{17}$$

where $\bar{\bar{C}}$ is the total penalty energy function added to the potential energy system for Eq. (16), $\bar{\bar{C_p}}$ is the courant function and γ_p is the penalty weight for interpolation equation p which must be defined. The augmented potential energy for the system is taken as $\bar{\bar{\Pi}} = 1/2\bar{\phi^t}\bar{\bar{K}}\bar{\phi} - \bar{\phi^t}\bar{b} + \bar{\bar{C}}$ where $\bar{\bar{K}}$ is the resulting matrix and $\bar{b}$ is the resulting source term from Eq. (16). Extremizing the augmented potential energy to minimize ϕ and the potential energy results in the penalized form of the equations

$$\begin{aligned} &-\sum_{faces} \frac{\phi_{nbr} - \phi_{cv}}{d_f} dA_f + \sum_{i.cons} \sum_{i.cvs} \gamma_p \alpha_{cv} \alpha_{i.cv} \phi_{i.cv} = -\sum_{face} u^{*,n} dA_f, \\ &\sum_{b.faces} \frac{-\phi_{nbr} + \phi_{cv}}{d_f} dA_f = 0, \\ &-\sum_{i.faces} \frac{\phi_{nbr} - \phi_{cv}}{d_f} dA_f - \sum_{i.cvs} \gamma_p \alpha_{cv} \alpha_{i.cv} \phi_{i.cv} = 0, \end{aligned} \tag{18}$$

where $\alpha_{i.cv}$ is the interpolation weights for interpolation cv $i.cv$ and the penalty functions are summed over all constraints allowing multiple constraints per cv. γ_p is a mesh dependent constant which must be defined in the equations to yield a consistent and accurate enforcement of the interpolation between meshes. Noting that $\alpha_{cv} = 1$ for interpolation cvs and taking $\gamma_p = f(d_f, dA_f)$

$$-\sum_{i.faces} \frac{\phi_{nbr} - \phi_{cv}}{d_f} dA_f - \sum_{i.faces} \frac{\sum_{i.cvs \neq cv} \alpha_{i.cv} \phi_{i.cv} - \phi_{cv}}{d_f} \tilde{\gamma} dA_f = 0, \tag{19}$$

where now $\tilde{\gamma} > 0$ is a specified constant which when increased results in a more accurate enforcement of the interpolated boundary condition. The resulting equations using this definition are symmetric, positive-definite, and non-singular. As $\tilde{\gamma}$ is increased the system becomes increasingly more singular, resulting in a more difficult system to solve. In numerical tests it is found that moderate values of $\tilde{\gamma}$ results in accurate enforcement of the interpolated boundary conditions such that the resulting linear system is readily solvable.

Eq. (19) is similar in form to other work that has used penalized formulations to enforce boundary conditions in work on finite element methods [36–38]. In such works, Dirichlet boundary conditions are enforced weakly using a mixed boundary condition, $\beta \frac{\partial \phi}{\partial n} + \chi(\phi - \phi_{bc}) = 0$, where β and χ must be selected to yield accurate enforcement of the desired boundary condition ϕ_{bc}. Dividing by β and setting $\chi/\beta \propto h^n$ is found to yield a system which is consistent and accurate, where h

is a mesh measure such as element radius and n is a constant found by an error bounds analysis. The expression used in Eq. (19) corresponds to the case where $n = -1$ and ϕ_{bc} is the interpolated value of ϕ.

The magnitude of the penalty on the linear system increases as meshes are refined as d_f^{-1} such that the interpolated boundary condition will be increasingly better enforced with increased resolution. The interpolation constraints are only exactly satisfied in the limits of infinite resolution and as such are never exactly enforced. If the error of a constraint is considerable, the penalized terms in Eq. (18) will result in locally high divergence values since $\sum_{faces} \frac{\phi_{nbr} - \phi_{cv}}{d_f} dA_f \neq \sum_{face} u^{*,n} dA_f$. This can result in instability within the method if care is not taken to ensure that the interpolation constraints are adequately enforced by having appropriate mesh resolution and proper selection of $\tilde{\gamma}$.

Summing all of the equations for a single mesh results in

$$\sum_{i.faces} \frac{\sum_{i.cvs \neq cv} \alpha_{i.cv} \phi_{i.cv} - \phi_{cv}}{d_f} \tilde{\gamma} dA_f = \sum_{i.+b.faces} u^{*,n} dA_f, \tag{20}$$

where here $i.faces$ refers to all faces along interpolation boundaries and $i.+b.faces$ refers to all boundary faces for a given mesh. For the expression to be consistent it is necessary that $\sum_{i.+b.faces} u^{*,n} dA_f = 0$. A similar result is found for single mesh methods where $\frac{\partial \phi_{bc}}{\partial n} = 0$ implies that $\sum_{b.faces} u^{*,n} dA_f = 0$. One could distribute a source/sink term such that Eq. (20) equates to zero. Similar strategies have been employed in IBM when using a discrete forcing to ensure good mass behavior near the surfaces of bodies [39]. A simple strategy would be to select a uniform source or sink to be distributed across an entire mesh. This would satisfy Eq. (20) but would introduce a non-local increased error which could potentially have a non-trivial affect on the local mass behavior of the method. In the present method a source term is instead introduced into the interpolation equations. This choice results in

$$-\sum_{i.faces} \frac{\phi_{nbr} - \phi_{cv}}{d_f} dA_f - \sum_{i.faces} \frac{\sum_{i.cvs \neq cv} \alpha_{i.cv} \phi_{i.cv} - \phi_{cv}}{d_f} \tilde{\gamma} dA_f = \epsilon, \tag{21}$$

where ϵ is the uniform distributed source term over all interpolation equations for a mesh, found such that Eq. (20) equates to zero. Effectively, ϵ is the mass flow rate of the predicted velocity field within a mesh distributed across interpolation boundaries. When $\tilde{\gamma} << 1$ the gradient of ϕ at interpolation boundaries will balance the distributed mass flow rate which is a statement of mass conservation over a mesh. As before, when $\tilde{\gamma}$ is increased the interpolation constraint is increasingly enforced. The introduction of ϵ to the interpolation equations is found in all cases presented to produce more accurate pressure fields than a non-local source/sink term.

To summarize a time step, Eq. (6) is solved where boundary conditions, interpolated or otherwise, are directly inserted into the expressions and a monolithic solve is performed for the entire linear system including all meshes. Eq. (18) is then solved using the interpolation boundary condition Eq. (21) over all meshes in a single monolithic solve. The cell-centered $-\frac{\partial \phi_{cv}^k}{\partial x_i}$ is reconstructed using Eq. (11). Fluid flow values of velocity and pressure for the next time step are then calculated according to Eq. (7). The same methodology is used to perform LES using the filtered equations.

3. Solid phase

The solid bodies are assumed to be rigid with arbitrary translation and rotation. Hydrodynamic forces and moments are directly integrated along surfaces and used to solve

$$m_b \frac{du_{b,i}}{dt} = \int_{\partial \Omega_b} \tau_{ij} n_j dA + m_b \left(1 - \frac{1}{m^*}\right) g_i + F_{coll,i}, \tag{22}$$

$$I_{ij} \frac{d\omega_j}{dt} + \epsilon_{ikl} \omega_k I_{lm} \omega_m = \int_{\partial \Omega_b} \epsilon_{ikl} r_k \tau_{lj} n_j dA, \tag{23}$$

$$\frac{dq_i}{dt} = \frac{1}{2} R_{ij} \omega_j. \tag{24}$$

The hydrodynamic forces on a body's surface ($\partial \Omega_b$) are discretely integrated using the incompressible stress tensor including pressure and viscous components (τ_{ij}). Buoyancy is included in Eq. (22) using the mass of an object (m_o), the body-to-fluid density ratio (m^*), any collisions forces $F_{coll,i}$ and the gravitation acceleration vector (g_i). Eq. (23) is a statement of conservation of angular momentum. The equation is solved in the principal orthogonal coordinates of the body about an axis centered at its center of mass. Hydrodynamic moments are integrated along $\partial \Omega_b$ using a moment arm r_k to the center of mass of a body. Here, ϵ_{ikl} is the Levi-Civita symbol, I_{ij} is the moment of inertia tensor with the principal moments of inertia as the diagonal, and ω_i is the rotational angular velocity about the principal axes. Eq. (24) is the equation of rotational orientation using the quaternion q_i to describe the orientation. To solve Eq. (24), a transformation matrix (R_{ij}) which is dependent on the components of q_i is used. To define R_{ij} and to integrate the rotational equations with time, we

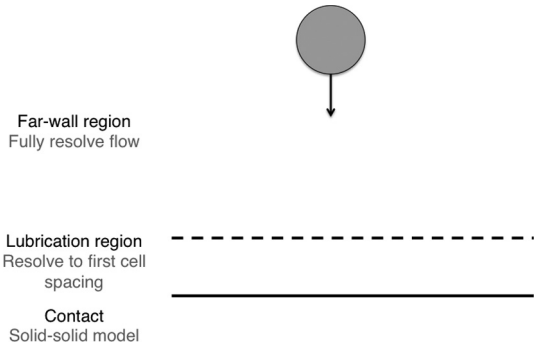

Fig. 7. Spherical particle colliding with a wall. Different flow regions (–) and corresponding modeling strategies (–) are shown for different particle locations.

follow the work of Murman et al. [40] who used a similar formulation to study the motion of a projectile separating from an aircraft. Translation is advanced in time using a $O(\Delta t^2)$ Taylor series expansion and RK4 time advancement is used for rotation. Multi-stepping is used for collisions where multiple solid body time steps are advanced per fluid time step during a given fluid motion time step. This is done to accurately capture the rapid changes which can occur during collisions.

Quaternions are four vectors which provide orientation information in a frame universal manner. Quaternions offer several advantages to other rotation orientation representations, such as Euler angles. They do not require any trigonometric calculations, are generally more compact, vary smoothly in rotational space, and avoid gimbal locking [41]. The formulation used in this work retains these properties and also avoids the need to recalculate any angular properties over time since the equations are defined in principal orthogonal coordinates. Additionally, complex rotational motions such as precession can be directly captured using the formulation.

Collisions between particles is a common feature in fluid flows of interest to PR-DNS. In the present work a linear spring-damper model is used for solid-solid body contact. This selection has been found by other work on PR-DNS to produce accurate results for cases with collisions [7,42]. In general collisional time scales are much shorter than fluid flow time scales. If the fluid flow is advanced at the collisional time scales, simulations become quickly intractable. If the motion of particles are rapidly changed within a fluid flow time step, the resulting fluid motion can potentially be numerically unstable. In the present method, similar to the work of Costa et al. [42], collisions are stretched over a fixed, specified number of time steps. As shown in the referenced work and as will be shown in this work, good accuracy is found using this selection.

To illustrate how collisions are handled in the current method, consider a smooth spherical particle colliding normally with a planar wall as depicted in Fig. 7. As the particle approaches the wall in the far-wall region the flow features are directly resolved and wall-induced hydrodynamic forces directly applied. As the particle nears the wall a lubrication layer forms between the wall and particle which imposes a force on the particle which is singular at the wall. Due to this singular forcing, the particle stops a small distance away from the wall before rebounding. Rather than directly resolving this small distance, which can be O(1 nm) for real particles, the current method truncates the singular force to one particle-surface cell spacing. Given the generally high resolution the method provides at the surfaces of particles this is expected to be a reasonable approximation. If the particle moves past the single cell spacing and intersects the wall, a solid-solid contact model is applied.

The solid-solid contact is chosen to be a linear spring-damper given by

$$F_{coll,i} = -\mu \Delta u_{s,i} - k \Delta x_{pen,i}. \tag{25}$$

Here $F_{coll,i}$ is the imposed collision particle in the ith Cartesian direction, μ is a empirical viscous damper coefficient, k is a empirical spring constant, $\Delta u_{s,i}$ is the difference in velocity of the two colliding surfaces, and $\Delta x_{pen,i}$ is penetration distance of the two colliding bodies. To complete the model μ and k must be provided. Following the work of Costa et al. [42], a solid-solid coefficient of restitution, ϵ_r, is specified and the collisions is set to occur over a known amount of time steps, $n\Delta t$, analytical forms of μ and k are found to be

$$\begin{aligned} k &= \frac{m_e(\pi^2 + ln^2\epsilon_r)}{n\Delta t^2}, \\ \mu &= -\frac{2m_e ln\epsilon_r}{n\Delta t}, \end{aligned} \tag{26}$$

where $m_e = (m_i^{-1} + m_j^{-1})^{-1}$ is the effective mass based on the mass of bodies i and j.

To couple the motion of the body and the fluid a weak coupling is used where the forces used to move bodies are taken from previous fluid flow information to produce the mesh velocity needed for ALE (u_{mesh}). As has been noted by other work on PR-DNS, weak coupling has been found to potentially produce stability issues for energetic, light bodies [16]. For the current work, such numerical issues were not found over the cases presented. As a possible extension, a monolithic

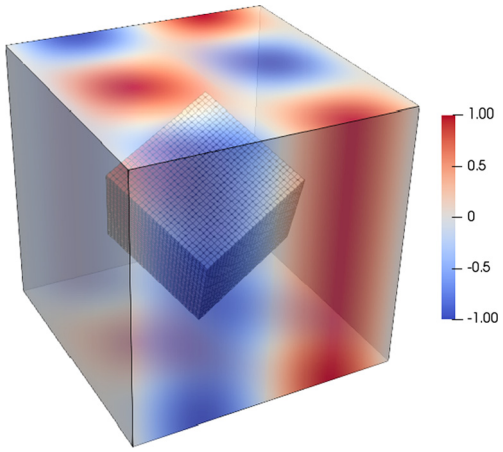

Fig. 8. Empty, tilted overset patch in periodic background with iso-contours of the x component of velocity for $Re = 100$ at physical time, $t = 0.1$. The background mesh dimensions and sizes are $L_x = L_y = L_z = 1$, $\Delta x = \Delta y = \Delta z = 1/80$ respectively. The overset mesh is half the size, has half the resolution in each direction, and is tilted on all three Euler angle axes by 25 degrees.

fluid/solid method, which solves both the fluid and solid body motion at once, could be constructed similar in principal to the monolithic method presented in Gibou and Min [43]. Such a method would ensure that time accurate solid body and fluid motion could always be achieved for energetic bodies.

4. Validation

4.1. Kinetic energy & order of accuracy

To demonstrate the kinetic energy properties of the supercell interpolant and the base method, a Taylor-Green vortex is simulated at different Re. A tilted, empty overset patch is placed within a periodic background mesh, as shown in Fig. 8. The resolution of patch and background mesh are adjusted to assess the convergence of the method. Re is varied to demonstrate the method's stability and accuracy at different levels of viscous dissipation.

The flow field is initialized with

$$\begin{aligned} u_{1,o} &= -cos(2\pi x)sin(2\pi y), \\ u_{2,o} &= sin(2\pi x)cos(2\pi y), \\ u_{3,o} &= 0, \end{aligned} \tag{27}$$

where $u_{i,o}$ is the initial velocity component in the ith direction, and the solution is stepped in time tracking the flow kinetic energy compared to the initial kinetic energy. Here, the resolution of the patch, given in Fig. 8, is selected to be significantly coarser than the background to illustrate the potential for energy generation in interpolation. The overlap, which can influence this result, is selected to be approximately 25% between the two meshes. The result is shown in Fig. 9 and compared to a local least-squares reconstruction interpolation result, similar to what has been employed in other overset methods. As can be seen the supercell results are stable even though there is effectively no viscous dissipation with $Re = 1e16$. Using a local LSQ reconstruction is unstable where kinetic energy is introduced through the interpolation building up over time. If one were to use a local reconstruction for this case, upwinding, limiters, or other numerical dissipation would possibly be necessary for robustness.

Fig. 10 depicts the kinetic energy from the overset solution compared to the analytical solution at varying values of Re. As can be seen in the figure, the method is able to accurately capture the analytical decay of kinetic energy over the range of Re investigated. This is true despite the presence of interpolation boundaries and non-trivial orientation of the meshes.

The introduction of interpolation and the penalty formulation maintains the order of accuracy of the base method for this case. To illustrate this, 4 simulations are conducted at a lower Re with different resolutions. As before, a tilted overset patch is placed in the center of the domain where now the meshes are chosen to be of the same resolution. The same $CFL = 0.25$ is chosen for each simulation and the resulting L_2 error is assessed for the fluid velocity and pressure at the same point in time according to the analytical solution

$$\begin{aligned} u_i &= u_{i,o}F(t), \\ p &= -\frac{1}{4}(cos(4\pi x) + cos(4\pi y))F(t)^2, \\ F(t) &= e^{-8\pi^2 \nu t}, \end{aligned} \tag{28}$$

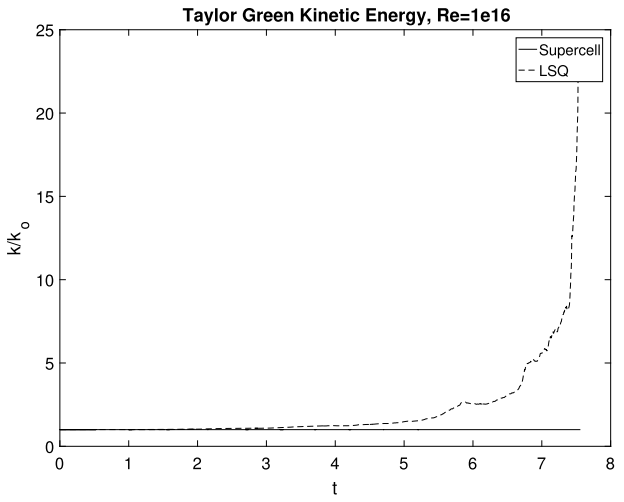

Fig. 9. Total kinetic energy, k, normalized by initial kinetic energy, k_o, of Taylor Green vortex at high Re using supercell and local LSQ interpolation.

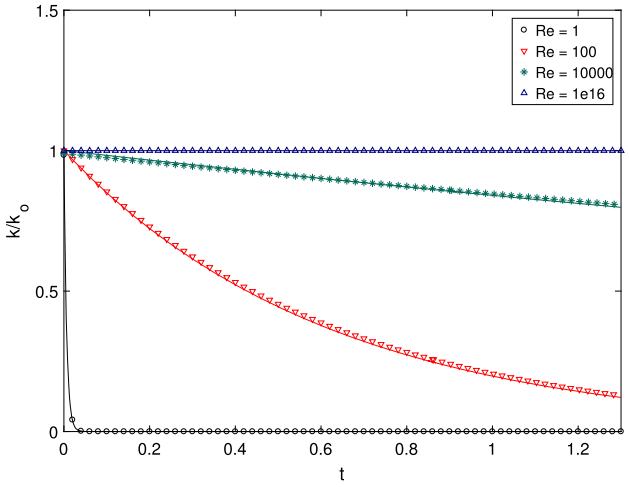

Fig. 10. Total kinetic energy, k, normalized by initial kinetic energy, k_o, of Taylor Green vortex at different values of Re. Symbols indicate simulation values and the lines indicate the analytical solution. Here, the meshes are of the same resolution, $\Delta = 1/80$, oriented as shown in Fig. 8.

where $F(t)$ decays the solution in time according to an exponential. Fig. 11 shows the resulting L_2 error at different resolutions. As is shown in the figure, $O(\Delta x^2)$ accuracy is found for the fluid velocity and pressure even with the introduction of the interpolation boundaries and the penalty formulation. The penalty weight, $\tilde{\gamma}$, is chosen to be 10. This illustrates that even with a relatively moderate value of penalty weight, good solutions can be found for this case.

4.2. Particles settling in quiescent fluid

Particles settling in quiescent fluid have previously been used to assess the accuracy of PR-DNS [16,7]. Spherical particles are released from rest and the resulting particle trajectory and flow field are compared to previous studies [12,44,45]. Depending on the Galileo number, Ga, and the particle-to-fluid density ratio, m^*, substantially different flow fields and trajectory character are found. For this study, the density ratio is fixed with $m^* = 7.8$ and Ga is varied over several particle motion regimes. Low Ga regimes which feature steady-state solutions and moderate Ga which feature chaotic, unsteady solutions are selected.

The domain is shown in Fig. 12. The mesh dimensions and resolutions are reported in Table 1. The Cartesian dimensions of the background domain, e.g. L_x, are given in terms of particle diameter, d_p. The uniform mesh spacing within the background domain mesh are given, e.g. N_x, and the near particle surface spacing per diameter, N_p/d_p. The two lowest values of Ga reported in the table exhibit steady state solutions while the two higher values are unsteady. Flow quantities are reported according to non-dimensional quantities $\widetilde{u} = \sqrt{|1 - m^*|gd_p}$ as a velocity scale, $\widetilde{t} = \sqrt{d_p/|1 - m^*|g}$ as a time scale and $\widetilde{x} = d_p$ as a length scale, matching parameters used in past work and including gravitational acceleration, g [12].

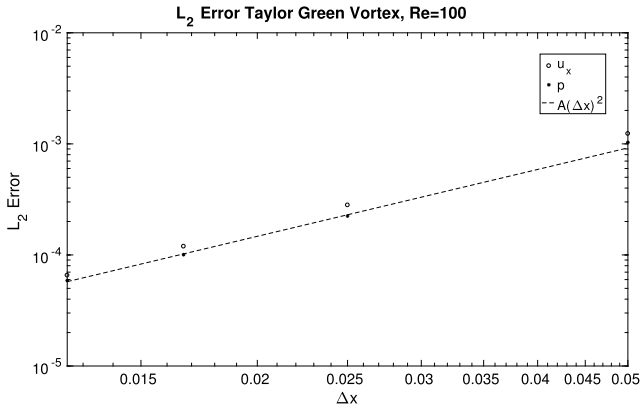

Fig. 11. L_2 error in streamwise velocity and pressure at different resolutions for Taylor Green vortex.

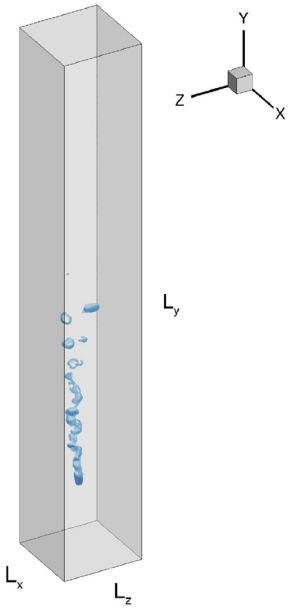

Fig. 12. Domain with λ_2 iso-volumes for $Ga = 500, m^* = 7.8$.

Table 1
Simulations.

Ga	m^*	L_x, L_y, L_z	N_x, N_y, N_z	N_p/d_p
1.2	7.8	$25d_p, 25d_p, 25d_p$	250, 250, 250	20
48.4	7.8	$15d_p, 80d_p, 15d_p$	450, 2400, 450	50
291	7.8	$15d_p, 100d_p, 15d_p$	450, 3000, 450	100
500	7.8	$15d_p, 100d_p, 15d_p$	450, 3000, 450	200

The size of overset grids are selected to be $4d_p$ in size. The near-surface resolution and background grid size are determined by preliminary simulations. The resulting meshes used for the case of $Ga = 500$ are shown in Fig. (13). Particles are simulated falling from rest using several meshes of increasing resolution. Simulations are run until the time-averaged total force was equal to 0 over a time period $t/\widetilde{t} = 10$. The drag force, F_d, on particles is time averaged over this same time period at the end of each simulation. The mesh which yields a relative change in average drag force, $\Delta F_{d,rel}$, less than 1% is selected. This process is performed for each particle in Table 1.

The boundary conditions for the background domain are selected to be zero-Neumann. To ensure that confinement effects are negligible, domain size was increased until flow disturbance along the domain boundaries were less than 1% of the maximum fluid velocity within a given simulation. This was particularly important for $Ga = 1.2$, which has $O(1/r)$ fluid disturbances at a radial distance r away from the particle surface, due to its strongly viscous character.

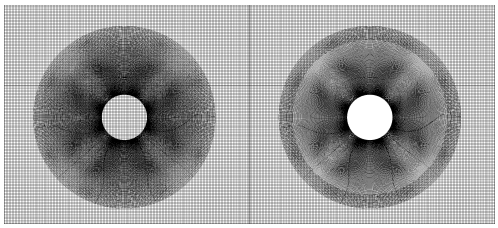

Fig. 13. Particle mesh on quiescent background mesh before and after overset assembly.

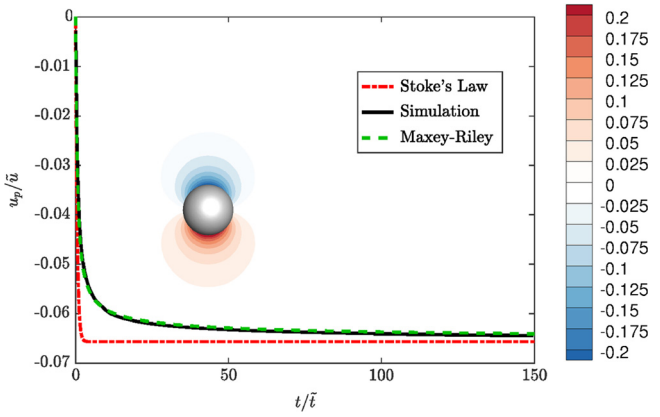

Fig. 14. $m^* = 7.8$, $Ga = 1.2$ Particle velocity solved using Stokes drag and gravity forces, from the simulation, and from using the Maxey-Riley equations. Contours of pressure at the end of the trajectory are shown with particle velocity.

For $m^* = 7.8$, $Ga = 1.2$ the particle is at a sufficiently low Re such that the steady-state hydrodynamic drag force on the particle can be estimated using Stokes drag law with an Oseen Correction ($C_d = 24/Re(1 + 3/16Re)$). Using this relation and a force balance, it is found that at steady state $Re \approx 0.077$. At this relatively low value of Re the Maxey-Riley equations are expected to adequately describe the trajectory of the sphere [46]. Fig. 14 compares a simulation using the overset method compared to a solution from the Maxey-Riley equations with and without the inclusion of unsteady forces. As can be seen in the figure, good agreement to the full Maxey-Riley solution is found.

When $m^* = 7.8$ and $Ga = 48.4$ the particle produces a wake in the quiescent fluid. Analytical expressions are no longer available for comparison and experimental results are instead used. In Mordant and Pinton [44], spherical particles were dropped in a tank of quiescent fluid and the resulting vertical particle velocity was measured. It was found in the work that the ensemble-averaged trajectories over $Re = 40 - 7000$ can be reasonably described by

$$u_p = u_{ss}\left[1 - exp\left(-\frac{3t}{\tau_{95}}\right)\right]. \tag{29}$$

In this expression u_p is the vertical velocity of the particle, u_{ss} is the ensemble-averaged steady state vertical velocity of the particle, and τ_{95} is the time it takes for the particle reach 95% of u_{ss} from no motion.

The overset method is used to simulate a spherical particle settling from rest for $Ga = 48.4$ and $m^* = 7.8$. The resulting trajectory is compared to Eq. (29) in Fig. 15. Good agreement to the experiment fit is found from the simulation data. The flow is laminar and the particle velocity steady at long integration times. Using the Galilean invariance property of the equations, the steady-state solution is compared to flow over a sphere. The resulting streamlines and vortex locations are compared to Johnson and Patel [47] in Fig. 16. It is found that the vortex locations and streamlines are in good agreement with their work for this case.

When Ga is increased to $Ga = 291$ or 500 the resulting particle trajectories are chaotic and unsteady. The flow field features unsteady vortices which interact with the particles causing unsteady motion. Trajectory results from the overset method are compared to Eq. (29) in Fig. 17 for 291 and Fig. 18 for 500. The resulting trajectories are both found to be in agreement with the experimental fit. In particular the time-averaged steady state particle velocity over the last $t/\tilde{t} = 10$ of the shown trajectories are found to be within 1% of the experimentally found u_{ss} as reported in Mordant and Pinton [44].

Substantial vortex distortion can occur as shed vortices pass through overset interpolation boundaries if significant interpolation error is introduced. To show the method's effectiveness of resolving complex fluid flow structures when overset interpolation boundaries are present, a shedding event is depicted for both values of Ga in Fig. 19. As can be seen in the

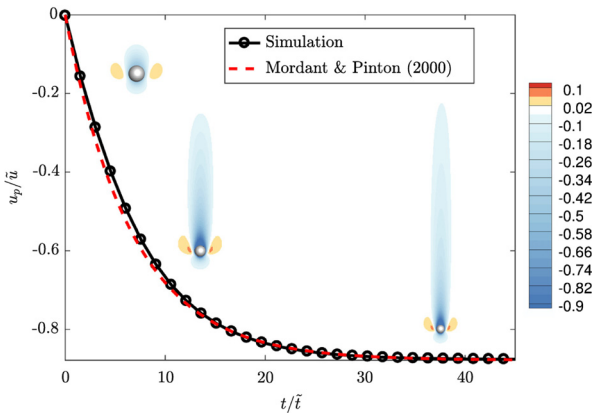

Fig. 15. $m^* = 7.8$, $Ga = 48$ Particle vertical velocity from the simulation and from the exponential fit from Mordant and Pinton [44].

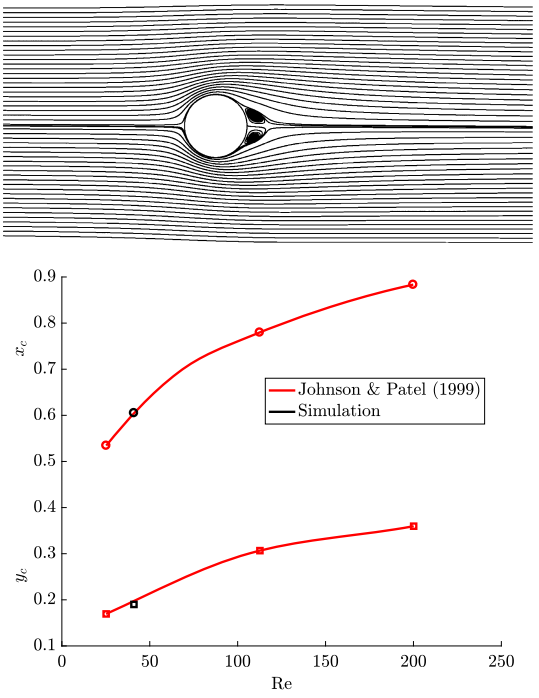

Fig. 16. $m^* = 7.8$, $Ga = 48$ Stream lines and vortex locations at $t/\tilde{t} = 40$ compared to Johnson and Patel [47] using Galilean invariance.

result no noticeable vortex distortion is found. Additionally, the expected hairpin structure is found for $Ga = 291$, as has been reported in previous work [45,12].

The cases presented in this section span a large range of Re and wide variety of particle motion regimes. In general good agreement is found for all cases presented when compared to experimental data and previous simulation work. This illustrates the method's effectiveness of accurately capturing particle and fluid motion over a wide range of regimes.

4.3. Collisions

Particle collisions influence the physics of many particle-laden flows. In particle-laden turbulent channel flow collisions are found to decrease particle concentrations near walls and play a significant role in the dissipation of fluid turbulence [48]. To demonstrate the effectiveness of the collision strategy used by this work, a spherical particle colliding against a planar wall is simulated and compared to reference experimental data.

First a low collisional $Re = 0.1$, case is considered. Here the lubrication layer dissipates all of the energy from the particle resulting in a zero effective coefficient of restitution. A spherical particle approaching a smooth, planar wall is simulated using the overset method. The resulting trajectory compared to experimental results from Gondret et al. [49] and

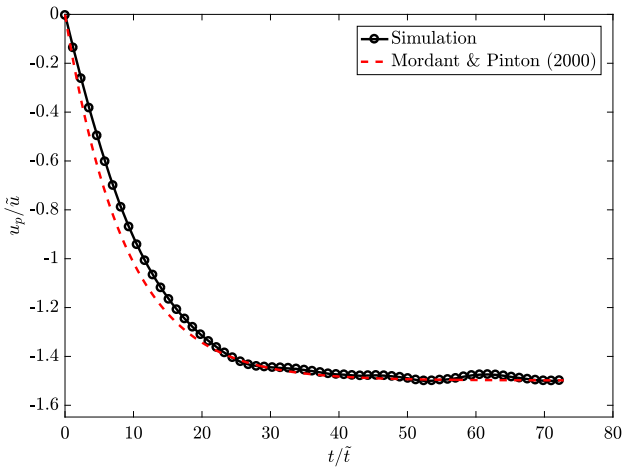

Fig. 17. $m^* = 7.8$, $Ga = 291$ Vertical particle velocity compared to the exponential fit from Mordant and Pinton [44].

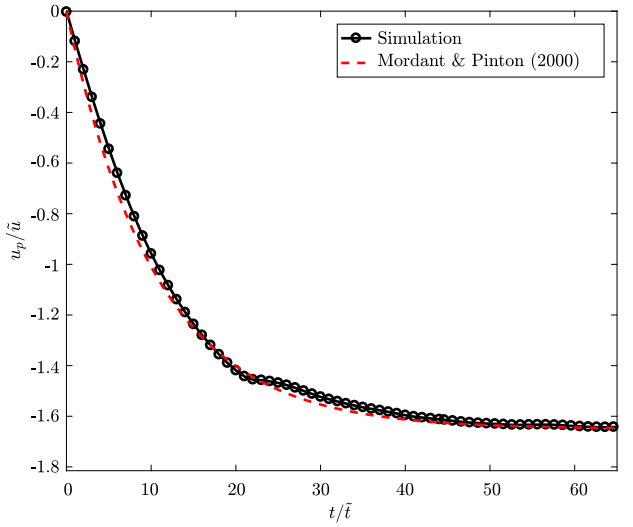

Fig. 18. $m^* = 7.8$, $Ga = 500$ Vertical particle velocity compared to the exponential fit from Mordant and Pinton [44].

the measured forces compared to the analytical Brenner force are shown in Fig. 20 [50,49]. As can be seen in the result, a zero effective coefficient of restitution is recovered even though the near-surface control volume spacing is inadequate to fully capture the lubrication layer for this case. Additionally, the hydrodynamic forces agree well with the Brenner forcing result. To show the effectiveness of the method when rebound occurs, a simulation is conducted for a more moderate $Re = 82$ with collisional Stokes number, $St = 152$. The resulting particle with time is compared to experimental trajectory data from Gondret et al. [49] in Fig. 21. As can be seen in the results, good agreement is found to the experimental particle trajectory. Lubrication forces influence the collision for this case, yielding an effective coefficient of restitution, ϵ_{eff}, lower than the solid-solid coefficient of $\epsilon_s = 0.99$. The method is found to accurately capture the experimental coefficient for the first particle bounce with $\epsilon_{eff} = 0.79$ which is comparable to the experimental value of 0.78 [49].

4.4. 50,000 particles in a turbulent channel

Simulations are performed of 50,000 spherical particles in a turbulent vertical channel to demonstrate the method at large computational scales. The domain and mesh information is given in Table 2. The particles and channel meshes are partitioned and distributed across 96,000 computational cores. The particles are selected to be spheres of uniform diameter, D_p. L_x is the length of the domain with N_x control volumes in the given direction, D_p/Δ_{bg} is the number of control volumes per diameter on the background channel mesh, $N_{o,vol}$ is the number of control volumes on each overset mesh, D_p/Δ_e is the number of control volumes per diameter at the edge of each overset mesh, and D_p/Δ_s is the number of control volumes per diameter near the surface of the particles.

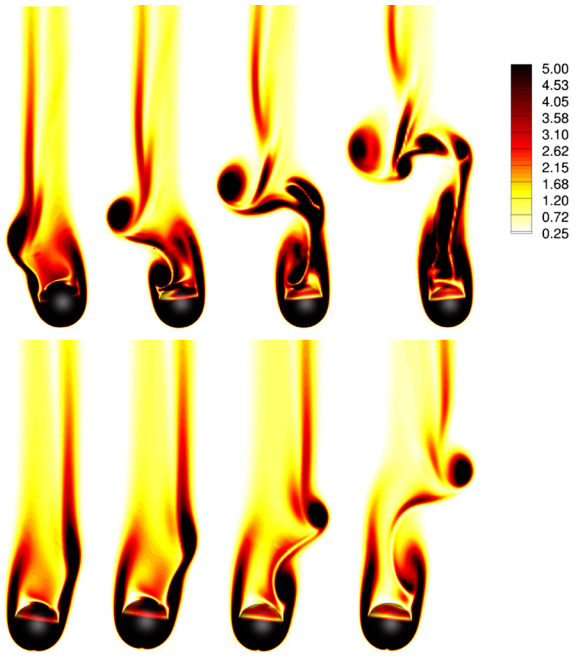

Fig. 19. Instantaneous contours of vorticity magnitude within a vortex shedding event for $Ga = 500$ followed by $Ga = 291$.

Table 2
Channel and overset mesh information.

$L_x \times L_y \times L_z$	$N_x \times N_y \times N_z$	D_p/Δ_{bg}
$4\pi \times 2 \times \pi$	$1934 \times 616 \times 967$	4

$N_{o,vol}$	D_p/Δ_e	D_p/Δ_s	D_p
15543	4	40	0.013

Table 3
Particle and channel non-dimensional parameters.

St_k	m^*	Re_τ	M	V
25	175	180	0.255	0.015

The particle Stokes number, St_k, particle-to-fluid density ratio, m^*, particle mass loading M, and particle volumetric loading V play significant roles in the motion of the fluid and particles. The selected parameters for this study are given in Table 3. Here, heavy inertial particles are selected at a relatively high value of Stokes number, $St_k = 25$. These selections will result in particle motion which can substantially differ from the fluid motion. In particular, moderate particle slip-velocity is expected near the walls of the channel, as found in other work in this regime [48,51].

A constant volumetric force is used to provide fluid flow at a friction Reynolds number of $Re_\tau = 180$. The flow is initialized with a laminar channel profile, at full Re_τ and with all 50,000 initially stationary particles. Flow disturbances, necessary for the transition to turbulence, are provided by the particles.

Instantaneous results of streamwise fluid velocity in the domain and particle surfaces are shown in Fig. 22. Flow and particle average streamwise velocity profiles are depicted in Fig. 23. Spanwise streak structures, a commonly noted flow feature in turbulent channel flow, are found in the instantaneous velocity fields near the wall. Particles are found to have substantially higher streamwise velocity near the channel walls. The average fluid velocity is found to match the clean channel flow. All of these results have been qualitatively found by previous experimental and numerical studies of particle-laden channel flow in similar regimes [51].

4.5. LES of P4381 propeller in crashback

The overset assembly, fluid and solid body motion methods presented in this work are readily useable for general bodies moving in incompressible, turbulent fluid. LES has successfully been used to study flow over moving, complex geometries such as flow over a P4381 propeller under crashback conditions [35,34,53]. To perform LES using the method, the filtered

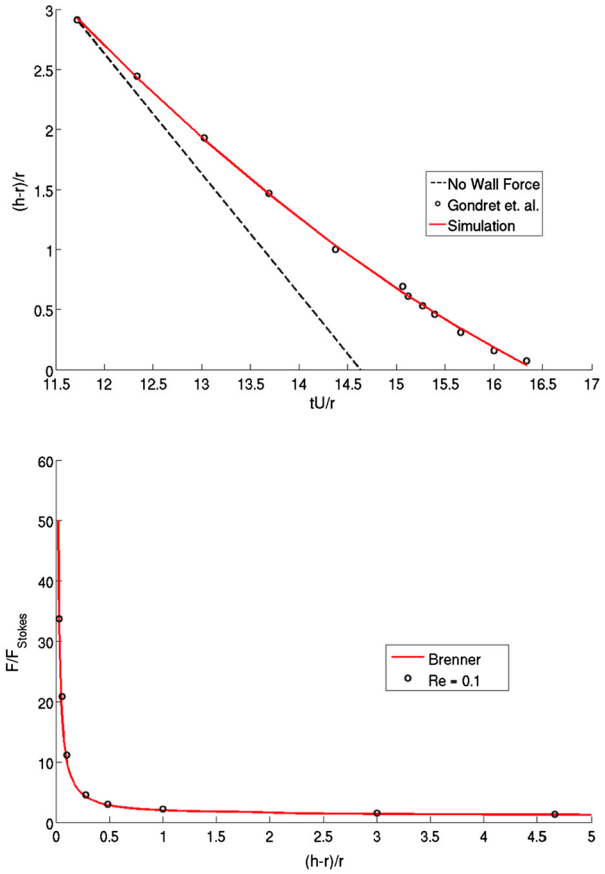

Fig. 20. Spherical particle colliding with a wall at collisional $Re = 0.1$. Hydrodynamic forces are shown compared to the analytical expression from Brenner [50] and the trajectory is compared to experimental results from Gondret et al. [49]. Here, h is the height of the center of the particle from the wall, r is the radius of the particle, F_{stokes} is the Stokes drag force without the wall, F is the hydrodynamic force, t is time scaled as necessary for comparison, and U is the particle velocity perpendicular to the wall. In the first figure, the symbols (o) indicate experimental results and the line indicates the simulation trajectory (–). In the second figure, the symbols (o) indicate forces measured from the simulation at different heights compared to the analytical Brenner wall force (–) [50].

Navier-Stokes equations are solved using the method. The dynamic Smagorinksy model is used to model the subgrid stress [54,55].

To demonstrate the method's LES capabilities, simulations are performed of a P4381 propeller under crashback conditions. In this case, the propeller rotates in reverse creating a reverse flow against a prescribed inflow condition. A large ring vortex is found near the vicinity of the blades which can chaotically shed causing large pressure forcing on the blades and shaft. Crashback features highly unsteady turbulent fluid flow over the complex propeller blade geometry, and is challenging when using an overset method. The vortex is expected to be located near interpolation boundaries. Errors due to interpolation and conservation must be small or significant error can be introduced repeatedly as flow circulates between interpolation boundaries in the vortex. Substantial errors at interpolation boundaries could disturb the vortex, potentially causing erroneous vortex shedding events which will result in incorrect pressure force predictions.

The simulation domain and meshes are depicted in Fig. 24. The time step was fixed with $dt = 0.004$. The domain and meshes were selected to match other simulation work which has successfully matched experimental data [53]. The overset mesh is chosen to be a hybrid mesh of tetrahedra, pyramids, and hexahedra to effectively mesh the complex, curved blade geometry. The background mesh is chosen to be a pure hexahedral mesh, which is suitable for its simpler geometry. An advance ratio of $J = v_{fs}/nD = -0.7$ at $Re = v_{fs}D/\nu = 480,000$ is chosen due to the ready availability of comparison simulation and experimental data. Here, v_{fs} is the imposed free-stream velocity, n is the rotations per second for the propeller and D is the propeller's diameter. To initiate the simulation, a uniform freestream velocity is used throughout the flow field with the propeller rotating at full rotation. Forcing statistics and average flow fields are taken after the initial flow transient over 300 propeller rotations.

Table 4 shows the non-dimensional thrust forces, side forces, and torque on the shaft and propeller over the averaging period. The average non-dimensional thrust force, K_t, torque, K_q, and root mean square, RMS, side force, K_s are compared in the figure to values from previous LES and experiments. It is found that the average forcing values agree well with previous work. In particular the non-dimensional thrust and torque is found to be within 3% of the reported value from

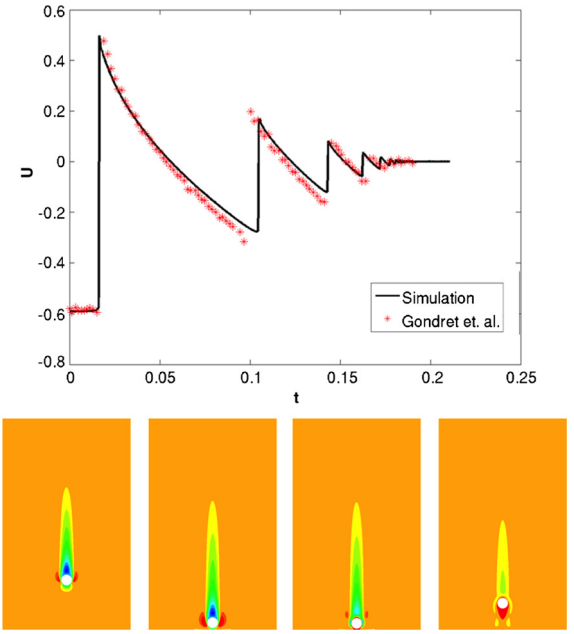

Fig. 21. Spherical particle colliding with a wall at $Re = 82$, $St = 152$, and $\epsilon_s = 0.99$ compared to Gondret et al. [49]. A trajectory comparison is shown with instantaneous iso-contours of vertical fluid velocity for the first rebound.

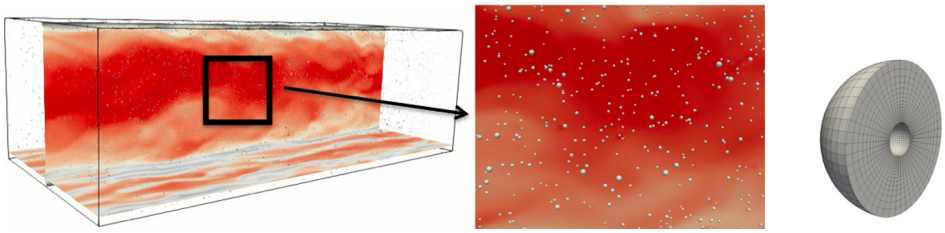

Fig. 22. Instantaneous contours of streamwise velocity with particle surfaces. Each surface shown in the result has the depicted mesh attached to it.

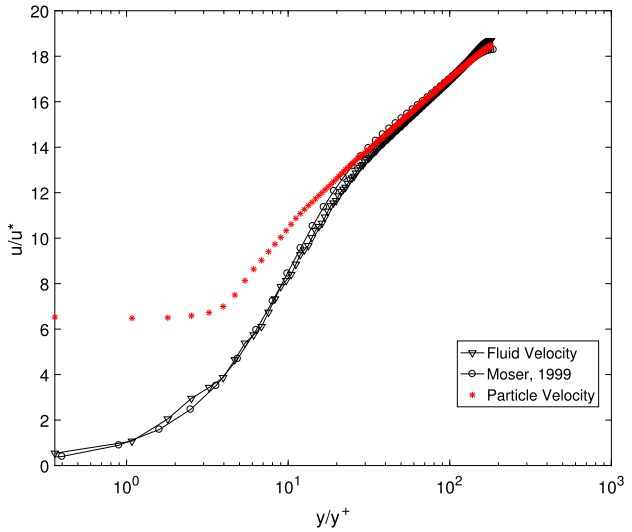

Fig. 23. Average streamwise velocity of simulated flow and particles non-dimensionalized with friction velocity, $u*$, with height non-dimensionalized by $y+$, compared to clean channel flow from Moser et al. [52].

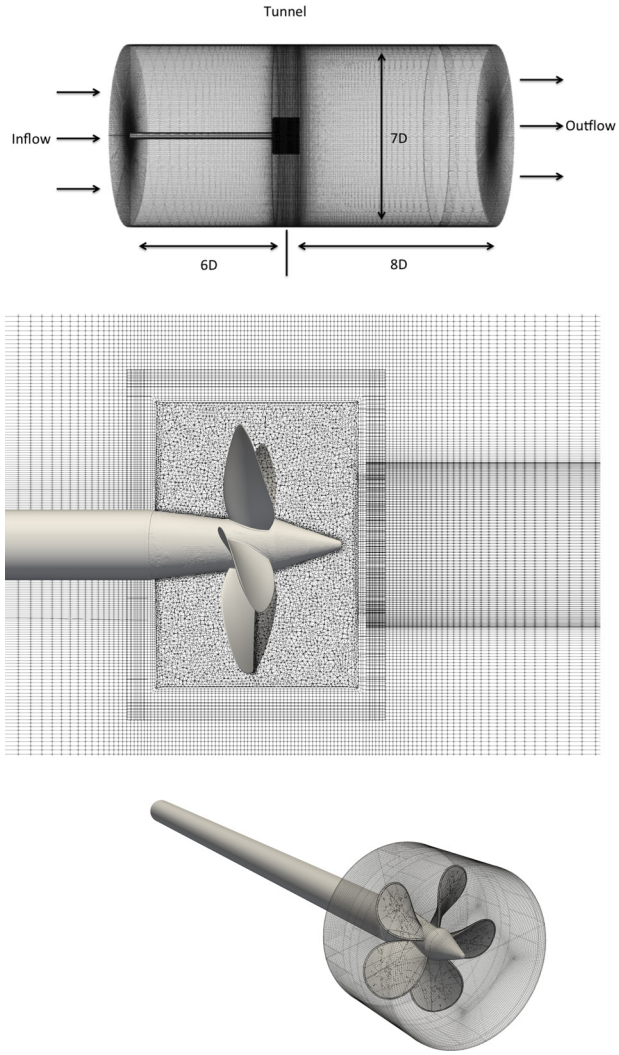

Fig. 24. Crashback domain and meshes. The total number of cells is 5 million within the background mesh and 3.6 million in the overset mesh. The overset mesh includes all 5 propeller blades and a portion of the end of the shaft. The background includes the tunnel, shaft, inflow and outflow surfaces. For boundary conditions a uniform inflow is prescribed and a zero fluid stress condition is enforced at the outflow and tunnel surfaces. The domain dimensions are as shown in the top figures. A vertical slice of the combined meshes after overset assembly is then shown, followed by a depiction of the overset mesh.

Table 4
Crashback forces.

	K_t	K_q	K_s
Jessup et al. [56]	−0.33	−0.065	0.030
Jang and Mahesh [53]	−0.39	−0.074	0.035
Ebert et al. [57]	−0.41	−0.078	–
Overset simulation	−0.41	−0.080	0.029

open water experiments [57]. The non-dimensional RMS of the side force is found to fall within 1% of data from water tunnel experiments [56].

Instantaneous flow fields are shown in Fig. 25. Qualitatively similar results are found in other simulation work for the instantaneous vortex shape and velocity field [53,34]. Looking at the circumferentially and time averaged flow field, as shown in Fig. 26, it is found that the shape, maximum and minimum values of velocity, and average vortex location match previous experimental and simulation results [53,34]. In particular, the average vortex location, $x/R = 0.89$ and $r/R = 1.69$, is found to be within 4% of previous water tunnel experiments, $x/R = 0.924$ and $r/R = 1.721$ [56].

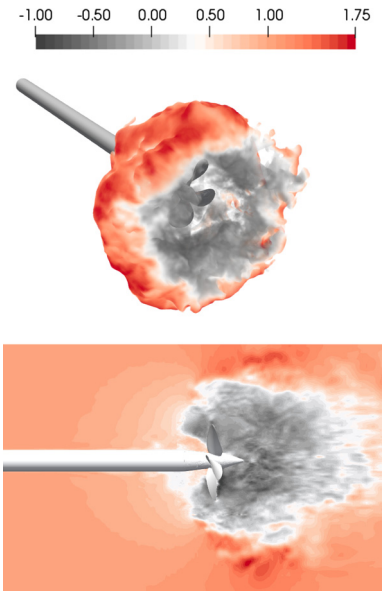

Fig. 25. Instantaneous velocity and pressure contours of flow over a P4381 propeller under crashback conditions. In the top figure, the ring vortex is shown using iso-surfaces of pressure colored by streamwise velocity. An instantaneous slice of streamwise velocity contours is then shown.

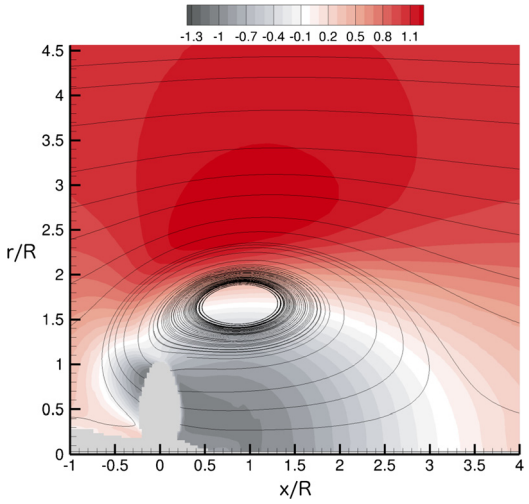

Fig. 26. Circumferentially and time averaged flow velocity and streamlines of flow over a P4381 propeller under crashback conditions. In the figure, R is the radius of the propeller, r is the radial direction chosen to be vertical, x is the streamwise direction chosen to be horizontal, and the azimuthal direction is chosen to be into the page. The average streamwise velocity contours are shown along with streamlines depicting the average vortex location.

5. Conclusions

Simulating moving bodies in turbulent fluid flows presents many numerical challenges. For a method to be successful it must resolve moving, dynamic boundary conditions efficiently and accurately. Motion is generally not known *a priori* making it difficult to ensure that adequate resolution is present in boundary layer regions along the surfaces of bodies. An overset method allows a guarantee of mesh resolution along body surfaces with the possible detriment of accuracy, especially in conservation, and computational cost related to connecting the solutions of overset meshes. The method presented here addresses these potential detriments by: using a mesh connectivity calculation method which is computationally efficient and can scale to large numbers of computational cores, introducing a novel supercell interpolant which has stable kinetic energy properties for interpolated quantities, and by using a penalty formulation to weakly enforce continuous pressure between meshes giving a controllable balance between mass conservation and direct interpolation.

Using these improvements, the method is able to maintain the order of accuracy of the numerical method and desirable kinetic energy properties for simulating turbulent fluid flows even with interpolated and reconstructed boundary conditions. DNS of many small moving bodies in turbulent fluid flow with collisions, as is required for PR-DNS, is clearly feasible using

the method. Good quantitative and qualitative agreement to previous experimental and simulation results was found over a variety of canonical particle-laden flow cases. These cases included spherical particles settling in quiescent fluid at a variety of Re, particles colliding with walls, and the computationally challenging case of 50,000 particles within a turbulent channel.

The presented method is additionally found to be suitable for LES/DNS of larger, complex bodies in turbulent fluid flows. This was demonstrated in this work by performing LES of flow over a P4381 propeller under crashback conditions. The physics of this case are non-trivial to capture in a simulation. Highly intermittent, unsteady turbulent fluid flow over complex moving geometry must be captured accurately over long integration times to get accurate forcing statistics. The method is found to be able to produce good agreement for challenging quantities such as the RMS of side force to experimental data and previous simulations.

In addition to being accurate, good flexibility is found in the design and construction of simulation domains and meshes. Often when performing a simulation of a complicated geometry a difficult part is creating a suitable computational mesh for the geometry. Breaking complex bodies into smaller, easier to mesh portions which no longer need to overlap and do not need to necessarily be the same resolution greatly simplifies this process. This provides great benefit even for simulations with no body motion.

Acknowledgements

The work was made possible by computational resources provided by Department of Energy as part of the Predictive Academic Alliance Program (PSAAP2) through the Department of Energy under DE-NA0002373. Further resources for this work were provided by the National Science Foundation (NSF) under NSF Grant CBET-1510154. Sreevatsa Anantharamu is gratefully acknowledged for providing the large channel mesh required for the particle-laden channel result. Praveen Kumar, Thomas Kroll and Karim Alame are acknowledged for creating meshes for use in the crashback simulations and for providing helpful input in using the method to perform LES.

References

[1] P. Mcleod, S. Carey, R.S.J. Sparks, Behaviour of particle-laden flows into the ocean: experimental simulation and geological implications, Sedimentology 46 (1999) 523–536.
[2] A. Lefebvre, Atomization and Sprays, Hemisphere, 1989.
[3] H. Chen, Y. Chen, H.T. Hsieh, N. Siegel, Computational fluid dynamics modeling of gas-particle flow within a solid-particle solar receiver, J. Sol. Energy Eng. 129 (2007).
[4] R.B. Stull, An Introduction to Boundary Layer Meteorology, vol. 13, Springer & Business Media, 2012.
[5] S. Tenneti, S. Subramaniam, Particle-resolved direct numerical simulation for gas-solid flow model development, Annu. Rev. Fluid Mech. 46 (2014) 199–230.
[6] S. Apte, M. Martin, N. Patankar, A numerical method for fully resolved simulation (FRS) of rigid particle-flow interactions in complex flows, J. Comput. Phys. 228 (2009) 2712–2738.
[7] A. Kidanemariam, M. Uhlmann, Interface-resolved direct numerical simulation of the erosion of a sediment bed sheared by laminar channel flow, Int. J. Multiph. Flow 67 (2014) 174–188.
[8] N. Sharma, N. Patankar, A fast computation technique for the direct numerical simulation of rigid particulate flow, J. Comput. Phys. 205 (2005) 439–457.
[9] T. Nomura, T. Hughes, An arbitrary Lagrangian-Eulerian finite element method for interaction of fluid and a rigid body, Comput. Methods Appl. Mech. Eng. 95 (1992) 115–138.
[10] P. Bagchi, S. Balachandar, Effect of turbulence on the drag and lift of a particle, Phys. Fluids 15 (2003) 3496–3513.
[11] T. Burton, J. Eaton, Fully resolved simulations of particle-turbulence interaction, J. Fluid Mech. 545 (2005) 67–111.
[12] M. Jenny, J. Dusek, G. Bouchet, Instabilities and transition of a sphere falling or ascending freely in a Newtonian fluid, J. Fluid Mech. 508 (2004) 201–239.
[13] N. Patankar, P. Huang, T. Ko, D. Joseph, Lift-off of a single particle in Newtonian and viscoelastic fluids by direct simulation, J. Fluid Mech. 438 (2001) 7–100.
[14] H. Choi, D. Joseph, Fluidization of 300 circular particles in plane Poiseuille flow by direct numerical simulation, J. Fluid Mech. 438 (2001) 101–128.
[15] C. Peskin, The fluid dynamics of heart valves: experimental, theoretical and computational methods, Annu. Rev. Fluid Mech. 14 (1981).
[16] M. Uhlmann, An immersed boundary method with direct forcing for the simulation of particulate flows, J. Comput. Phys. 209 (2005) 448–476.
[17] R. Glowinski, T.W. Pan, T. Hesla, D. Joseph, J. Périaux, A fictitious domain approach to the direct numerical simulation of incompressible viscous flow past moving rigid bodies: application to particulate flow, J. Comput. Phys. 169 (2001).
[18] K. Taira, T. Colonius, The immersed boundary method: a projection approach, J. Comput. Phys. 225 (2007) 2118–2137.
[19] R. Meakin, N. Suhs, Unsteady Aerodynamic Simulation of Multiple Bodies in Relative Motion, AIAA Paper 98, 1989, 1996.
[20] Y. Tseng, J. Ferziger, A ghost-cell immersed boundary method for flow in complex geometry, J. Comput. Phys. 192 (2003).
[21] R. Mittal, G. Iaccarino, Immersed boundary methods, Annu. Rev. Fluid Mech. 37 (2005).
[22] F. Sotiropolous, X. Yang, Immersed boundary methods for simulating fluid-structure interaction, Prog. Aerosp. Sci. 65 (2014).
[23] L. Zhu, C. Peskin, Interaction of two filaments in a flowing soap fill, Phys. Fluids 15 (2003).
[24] G. Iaccarino, R. Verzicco, Immersed boundary technique for turbulent flow simulations, Appl. Mech. Rev. 56 (2003) 331–347.
[25] Z. Wang, V. Parthasarathy, A fully automated chimera methodology for multiple moving body problems, Int. J. Numer. Methods Fluids 33 (2000) 919–938.
[26] W.J. Horne, K. Mahesh, A massively-parallel, unstructured overset method for mesh connectivity, J. Comput. Phys. 376 (2019) 585–596.
[27] H. Tang, S.C. Jones, F. Sotiropoulos, An overset-grid method for 3d unsteady incompressible flows, J. Comput. Phys. 191 (2003) 567–600.
[28] Z. Wang, A fully conservative interface algorithm for overlapping grids, J. Comput. Phys. 122 (1995) 96–109.
[29] K. Mahesh, G. Constantinescu, P. Moin, A numerical method for large-eddy simulation in complex geometries, J. Comput. Phys. 197 (1) (2004) 215.
[30] P. Moin, K. Mahesh, Direct numerical simulation: a tool in turbulence research, Annu. Rev. Fluid Mech. 30 (1998) 539–578.
[31] R. Mittal, P. Moin, Suitability of upwind-biased finite-difference schemes for large-eddy simulation of turbulent flows, AIAA J. 35 (1997) 1415.
[32] L. Timmermans, P. Minev, F. Van De Vosse, An approximate projection scheme for incompressible flow using spectral elements, Int. J. Numer. Methods Fluids 22 (1996) 673–688.

[33] J. Guermond, J. Shen, On the error estimates for the rotational pressure-correction methods, Math. Comput. 73 (2003) 1719–1723.
[34] A. Verma, H. Jang, K. Mahesh, The effect of an upstream hull on a propeller in reverse rotation, J. Fluid Mech. 704 (2012) 61–88.
[35] H. Jang, A. Verma, K. Mahesh, Predicting unsteady loads in marine propulsor crashback using large eddy simulation, Int. J. Rotating Mach. 2012 (2012).
[36] J.W. Barret, C.M. Elliot, Finite element approximation of the Dirichlet problem using the boundary penalty method, Numer. Math. 49 (1986) 343–366.
[37] I. Babuška, The finite element with penalty, Math. Comput. 27 (1973) 221–228.
[38] R. Becker, P. Hansbo, R. Stenberg, A finite element method for domain decomposition with non-matching grids, Math. Model. Numer. Anal. 37 (2003) 209–225.
[39] J. Kim, D. Kim, H. Choi, An immersed-boundary finite-volume method for simulations of flow in complex geometries, J. Comput. Phys. 171 (2001) 132–150.
[40] S. Murman, M. Aftosmis, M. Berger, 6-dof motion with a cartesian method, in: 41st AIAA Aerospace Sciences Meeting, 2003, volume AIAA-2003-1246.
[41] J. Wertz, D. Reidel Publishing Company, 1980.
[42] P. Costa, B. Boersma, J. Westerweel, W.-P. Bruegem, Collision model for fully resolved simulations of flows laden with finite sized particles, Phys. Rev. E 92 (2015) 053012.
[43] F. Gibou, C. Min, Efficient symmetric positive definite second-order accurate solver for fluid/solid interactions, J. Comput. Phys. 231 (2012) 3246–3263.
[44] N. Mordant, J.F. Pinton, Velocity measurement of a settling sphere, Eur. Phys. J. B 18 (2000) 343–352.
[45] M. Horowitz, C.H.K. Williamson, The effect of Reynolds number on the dynamics and wakes of freely rising and falling spheres, J. Fluid Mech. 651 (2010) 251–294.
[46] M.R. Maxey, J.J. Riley, Equation of motion for a small rigid sphere in a nonuniform flow, Phys. Fluids 26 (1983) 883–889.
[47] T. Johnson, V. Patel, Flow past a sphere up to a Reynolds number of 300, J. Fluid Mech. 378 (1999) 19–70.
[48] Y. Li, J.B. Mclaughlin, K. Kontomaris, L. Portela, Numerical simulation of particle-laden turbulent channel flow, Phys. Fluids 13 (2001) 2957.
[49] P. Gondret, M. Lance, L. Petit, Bouncing motion of spherical particles in fluids, Phys. Fluids 14 (2002) 643–652.
[50] H. Brenner, The slow motion of a sphere through a viscous fluid towards a plane surface, Chem. Eng. Sci. 16 (1961) 242–251.
[51] J.D. Kulick, J.R. Fessler, J.K. Eaton, Particle response and turbulence modification in fully developed channel flow, J. Fluid Mech. 277 (1994) 109–134.
[52] R.D. Moser, J. Kim, N.N. Mansour, Direct numerical simulation of turbulent channel flow up to $Re_\tau = 590$, Phys. Fluids 11 (1999) 943–945.
[53] H. Jang, K. Mahesh, Large eddy simulation of flow around a reverse rotating propeller, J. Fluid Mech. 729 (2013) 151–179.
[54] D.K. Lilly, A proposed modification of the germano subgrid-scale closure method, Phys. Fluids A, Fluid Dyn. 4 (1992) 633–635.
[55] M. Germano, U. Piomelli, P. Moin, W.H. Cabot, A dynamic subgrid-scale eddy viscosity model, Phys. Fluids A, Fluid Dyn. 3 (1991) 1760–1765.
[56] S. Jessup, C. Chesnakas, D. Fry, M. Donnelly, S. Black, J. Park, Propeller performance at extreme off design conditions, in: Proceedings of the 25th Symposium on Naval Hydrodynamics, St. John's, Canada, 2004.
[57] M. Ebert, P. Chang, L. Mulvihill, Nswccd fy07 crashback computational effort, ONR Propulsor S & T Program Review, October 2007.